RSC Advances

COMMUNICATION

View Article Online
View Journal | View Issue

Cite this: *RSC Adv.*, 2014, **4**, 48590

Received 17th June 2014
Accepted 22nd September 2014

DOI: 10.1039/c4ra05863a

www.rsc.org/advances

Controlled synthesis of $ZnGa_2O_4$ nanorod arrays from hexagonal ZnO microdishes and their photocatalytic activity on the degradation of RhB†

Zesheng Li,*[a] Bolin Li,[a] Zhenghui Liu,[a] Dehao Li,[a] Chunyu Ge[b] and Yueping Fang*[b]

Novel $ZnGa_2O_4$ nanorod arrays with desirable photocatalytic activity for organic dye degradation have been synthesized by an associated solution–liquid–solid growth and topological morphology-conversion synthetic strategy.

The manipulation of physical dimensions and chemical compositions of semiconductors has attracted intensive attention due to their important roles in determining the physicochemical properties of the materials.[1] The emergence and application of nanotechnology has provided great exciting advances in controlling the structure and morphology of semiconductors.[2] Among various nanostructures, one-dimensional (1-D) nanostructures, such as wires, tubes, rods and belts have attracted intense research interest because they exhibit outstanding properties in the optical, electronic, and catalytic fields.[3] Compared with conventional bulk materials and 0-D structures (*e.g.*, nanoparticles), 1-D nanostructures can improve the transport of charge carriers and thus reduce the recombination losses at grain boundaries.[4] Particularly, the aligned 1-D nanostructures formed by the directed self-assembly of nanorods, nanowires and nanotubes are a class of novel 1-D oriented architectures that gives rise to extraordinary collective properties.[5] Such self-supported 1-D arrays are demonstrated to have high performance in catalysis systems for the photocatalytic degradation of organic dyes[6] and for air purification[7] due to their large surface area, integrated charge-transfer paths, as well as morphological stability.[8]

As an important functional semiconductor with a direct wide band gap (3.37 eV) and a large exciton binding energy (60 meV), ZnO has attracted great interest owing to its potential applications in photocatalysis, solar cells, sensors, nanogenerators, room-temperature ultraviolet (UV) lasers, optical waveguides, and so on.[9] Recently, $ZnGa_2O_4$, a bimetallic semiconductor with spinel structure, has been investigated for its technical application in the photocatalytic field.[10] Because its hybridized orbits of Ga4s4p and Zn4s4p and wider band gap (4.4 eV), $ZnGa_2O_4$ can promote the mobility of photogenerated electrons and improve the absorption efficiency in UV light radiation, which is the most available light source for waste water purification by photocatalytic degradation.[11] Generally, 1-D $ZnGa_2O_4$ could be synthesized by chemical vapor deposition (CVD),[12] which requires a thin-film ZnO template and multiple steps of high-temperature processes (>1000 °C). It is believed that complicated methods of material synthesis are not advantageous for further applications.[13] For this purpose, a facile synthesis method for 1-D $ZnGa_2O_4$ nanostructures is highly desirable for their scalable application in photocatalytic fields.

It is well known that the solution–liquid–solid (SLS) growth mechanism has been widely applied to prepare various continuous 1-D crystalline nanostructures *via* hydrothermal synthesis routes, in which low-melting point metals (*e.g.*, In, Ga and Sn, *etc.*) are used to induce the growth of 1-D nanostructures.[14] Previously, we have developed the SLS method under hydrothermal conditions for the growth of Sn-filled $In(OH)_3$ nanotubes[15] and the twinned nanotowers and nanodendrites of HgSe.[16] Recently, we further developed a Ga-mediated SLS growth strategy for the synthesis of novel Ga-doped, self-supported, independent, aligned ZnO nanorods by one-pot hydrothermal synthesis.[17] Furthermore, the topological morphology conversion (TMC) process has proven to be a promising technique for the synthesis of newly nanostructured materials by means of chemical and structural transformation from established precursors with similar morphologies.[18] Most recently, we reported the synthesis of novel SnO_2-doped SiC hollow nanochains by TMC process from a precursor of SnO_2@C core–shell nanochains.[19]

[a]*Development Center of Technology for Petrochemical Pollution Control and Cleaner Production of Guangdong Universities, College of Chemical Engineering, Guangdong University of Petrochemical Technology, Maoming, Guangdong, 525000, China*
[b]*Institute of Biomaterial, College of Science, South China Agricultural University, Guangzhou, 510642, China. E-mail: lzs212@163.com; ypfang@scau.edu.cn*

† Electronic supplementary information (ESI) available. See DOI: 10.1039/c4ra05863a

In this study, we demonstrate the controlled synthesis of $ZnGa_2O_4$ nanorod arrays from hexagonal ZnO microdishes by using an efficient strategy utilizing SLS growth and TMC process. Firstly, the Ga-doped ZnO nanorod arrays were synthesized by the regular Ga-mediated SLS hydrothermal synthesis,[17] in which the hexagonal ZnO microdishes were transformed into aligned ZnO nanorods. Secondly, $ZnGa_2O_4$ nanorod arrays were further synthesized by a heat-treating TMC process from the Ga-doped ZnO nanorod arrays (see ESI† for detailed synthetic steps). The newly designed 1-D semiconductor nanostructures of $ZnGa_2O_4$ nanorod arrays showed a very high activity for the photocatalytic degradation of Rhodamine B (RhB) under UV light radiation.

The phase structures of the as-synthesized samples have been characterized by XRD. Fig. 1 shows the XRD patterns of the hexagonal ZnO microdishes (black pattern), Ga-doped ZnO nanorod arrays (red pattern) and the $ZnGa_2O_4$ nanorod arrays (blue pattern). From the black and red patterns, it can be readily concluded that the two samples have the hexagonal phase structures of ZnO (JCPDS card no. 36-1451 (ref. 9)). The sharp and clear diffraction peaks clearly indicate the good crystalline nature of the two products. It suggests that the ideal ZnO structures have been obtained by the hydrolyzation of $ZnSt_2$ under hydrothermal treatment. Expressly, from the red pattern, no obvious Ga diffraction peak can be observed for the Ga-doped ZnO sample, which is mainly due to the amorphous existence of Ga dopant as indicated by one of our previous works.[17] As illustrated by the blue pattern, the XRD pattern of the $ZnGa_2O_4$ sample can be indexed as cubic spinel $ZnGa_2O_4$ with a cell parameter of $a = 8.335$ Å, agreeing well with the JCPDS Card no. 38-1240.[10] Several distinct peaks at 30.31, 35.71, 43.41, 57.41 and 63.01 match well with the (220), (311), (400), (511) and (440) crystal planes of $ZnGa_2O_4$, respectively. There is negligible ZnO component that remained in the $ZnGa_2O_4$ sample. Therefore, the results indicate that the $ZnGa_2O_4$ phase has been successfully synthesized from the Ga-doped ZnO phase *via* the heat-treating conversion process.

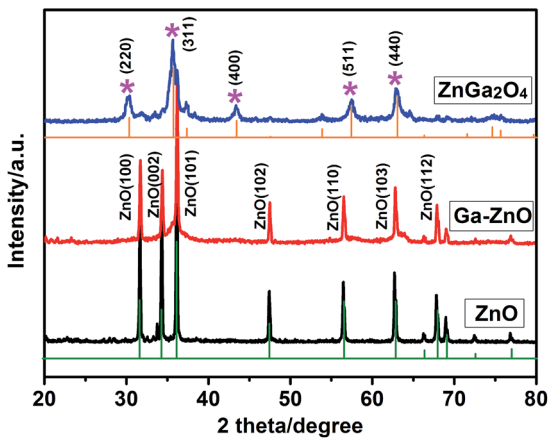

Fig. 1 XRD pattern of hexagonal ZnO microdishes (black), Ga-ZnO nanorod arrays (red) and $ZnGa_2O_4$ nanorod arrays (blue).

Schematic illustrations of crystal structures for $ZnGa_2O_4$ are illustrated in Fig. 2. The ball-and-stick model (Fig. 2A) shows the typical cubic unit cell of spinel $ZnGa_2O_4$, corresponding to the XRD data. Fig. 2B displays the crystallographic shear of $ZnGa_2O_4$, where zinc/oxygen tetrahedrons are shown in yellow. For one unit cell of $ZnGa_2O_4$, $32O^{2-}$ constitute the close-packed subunit cell with a face-centred-cubic structure, $8Zn^{2+}$ occupy 8 tetrahedral vacancies (accounting for 1/8 of the total number of tetrahedral vacancies) to form 4 A-sites, and $16Ga^{3+}$ occupy 16 octahedral vacancies (accounting for 1/2 of the total number of octahedral vacancies) to form 4 B-sites, where one complete unit cell of spinel $ZnGa_2O_4$ is made up of the 4 A-sites and 4 B-sites by alternate permutation.

To investigate the detailed nanostructures and morphological evolution of the as-prepared samples, FE-SEM and TEM characterization were further implemented. Fig. 3 shows the representative SEM images of the hexagonal ZnO microdishes. The lower-magnification images (Fig. 3A and B) indicate that the sample has an interesting configuration comprising homologous 3-D hexagonal microdishes. The higher-magnification images (Fig. 3C and D) reveal that the flowerpot is made up of a hexagonal pot on one side and short nanorods on the other (just like one flowerpot).

Fig. 4A and B show the representative SEM images of Ga-doped ZnO nanorod arrays. Evidently, the sample has highly self-supported, aligned 1-D nanostructures, where the ZnO nanorods are vertically well-assembled into micro-architectures without extraneous supporting substrates. These results demonstrate that ZnO 1-D nanostructures have been achieved by the Ga-mediated SLS hydrothermal process. Fig. 4C and D show the representative SEM images of $ZnGa_2O_4$ nanorod arrays, which reveal the loosely aligned 1-D nanostructures relative to the Ga-doped ZnO sample. Fig. 5 shows the SEM-EDS elemental mapping of Ga, Zn and O from the individual $ZnGa_2O_4$ nanorod array. It is found that the three elements, Ga, Zn and O (Fig. 5B–D), are homogeneously distributed, corresponding to the SEM image (Fig. 5A).

Fig. 6 shows the TEM images of Ga-doped ZnO nanorods (Fig. 6A and B) and $ZnGa_2O_4$ nanorods (Fig. 6C and D). It can be observed that the two samples both have dense, aligned nanorod architectures with single nanorods of 50–80 nm diameter. A spot of nanopores exists in the $ZnGa_2O_4$ nanorods (see Fig. 6D),

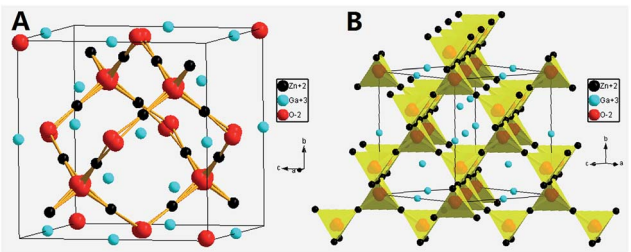

Fig. 2 Schematic illustrations of the crystal structures for $ZnGa_2O_4$: (A) a ball-and-stick model and (B) the crystallographic shear, zinc/oxygen tetrahedrons are showed in yellow.

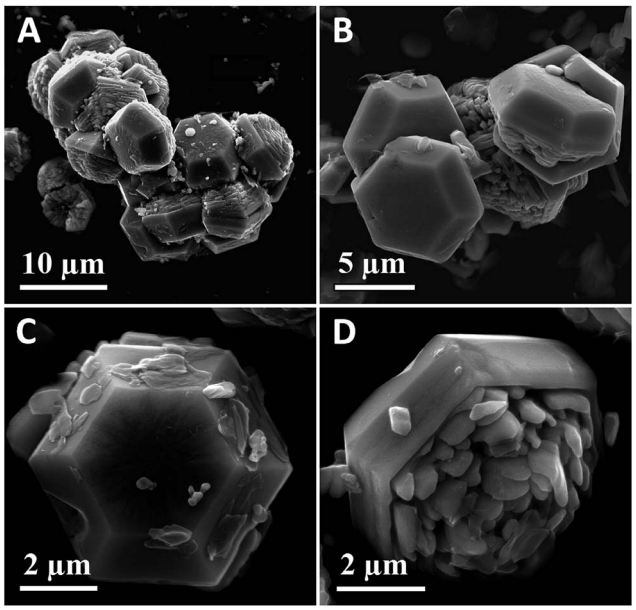

Fig. 3 Representative SEM images of hexagonal ZnO microdishes.

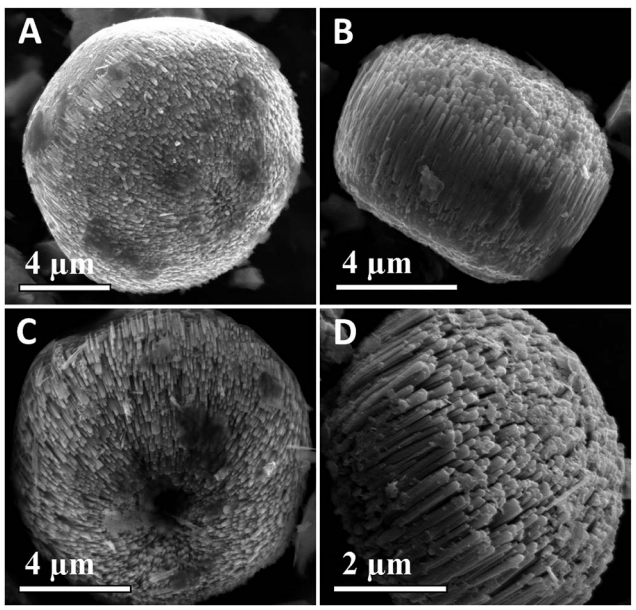

Fig. 4 Representative SEM images of the nanorod arrays: (A) and (B) Ga-ZnO, (C) and (D) $ZnGa_2O_4$.

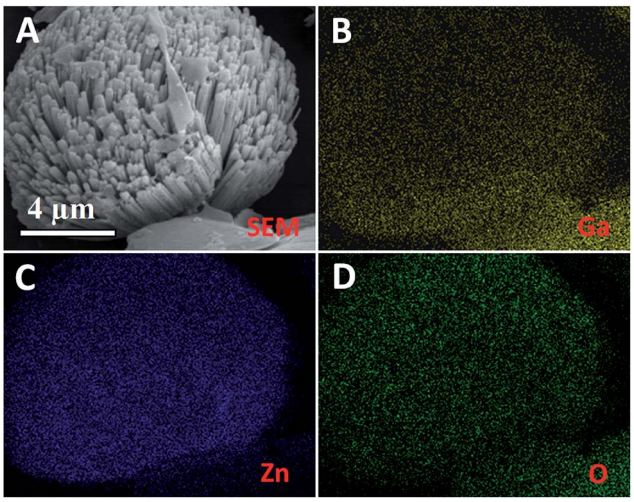

Fig. 5 SEM-EDS elemental mapping images from the $ZnGa_2O_4$ nanorod array.

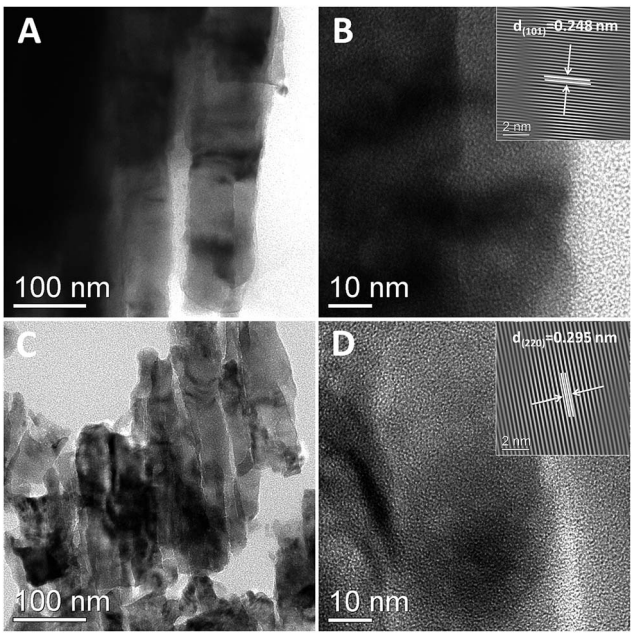

Fig. 6 TEM images of the (A) and (B) Ga-ZnO nanorods and (C) and (D) $ZnGa_2O_4$ nanorods.

which might originate from crystal defects during the structure conversion process. The insets in Fig. 6B and D further indicate the (101) planes of ZnO ($d = 0.248$ nm) and the (220) planes of $ZnGa_2O_4$ ($d = 0.295$ nm). The above-mentioned results largely demonstrate the feasibility of topological morphology conversion of Ga-doped ZnO nanorods to $ZnGa_2O_4$ nanorods by the TMC heat-treating process. In addition, the BET specific surface areas of $ZnGa_2O_4$ nanorods, Ga-doped ZnO nanorods and hexagonal ZnO microdishes were determined as 65.7, 61.2 and 38.4 $m^2\ g^{-1}$, respectively.

The possible formation process of the $ZnGa_2O_4$ nanorod arrays, involving the evolution of Ga-doped ZnO nanorods and $ZnGa_2O_4$ nanorods, are schematically shown in Fig. 7. In the absence of Ga during the hydrothermal process, hexagonal ZnO microdishes were obtained (see Fig. 3 for details), indicating the Ga species plays an important role in the formation of the ZnO 1-D framework.[17] Fig. 7 (i) illustrates a formation process of the Ga-doped ZnO nanorods with the SLS growth route. The SLS process may consist of four steps:[14] formation of the liquid Ga droplets in hydrothermal solution (S), production of ZnO by $ZnSt_2$ hydrolysis and its diffusion to liquid Ga droplet to form a liquid–solid (LS) interface, 1-D growth of the Ga-doped ZnO

Fig. 7 Schematic illustration for the preparation of $ZnGa_2O_4$ nanorods: (i) solution–liquid–solid (SLS) growth for Ga-doped ZnO nanorods and (ii) topological-morphology-conversion (TMC) process for $ZnGa_2O_4$ nanorods.

nanorods at the LS interface, and continuous 1-D growth of ZnO, consuming the liquid Ga droplet and thus completing the SLS assembly of the Ga-doped ZnO nanorods. Fig. 7 (ii) illustrates the latent evolution of the $ZnGa_2O_4$ nanorods from Ga-doped ZnO nanorods in the TMC process. In this process, the initial nanorod morphology of the Ga-doped ZnO precursor would be inherited by the $ZnGa_2O_4$ product by means of the potential chemical and structural transformation (ZnO reacting with Ga to form $ZnGa_2O_4$) under the heat-treating process. Further study on the accurate reaction mechanism is in progress.

The photocatalytic activities and stability of the as-prepared photocatalysts (the $ZnGa_2O_4$ nanorods, Ga-doped ZnO nanorods and hexagonal ZnO microdishes) were evaluated by degradation of RhB in aqueous solution under UV light radiation (see Fig. 8). Obviously, the $ZnGa_2O_4$ nanorods exhibit a much higher photocatalytic activity than the Ga-doped ZnO nanorods and hexagonal ZnO microdishes (Fig. 8A). RhB was largely degraded (97.2%) in 90 min under UV light radiation, while the degradation rates of Ga-doped ZnO nanorods and hexagonal ZnO microdishes were only 75.9% and 57.1%, respectively. The first-order reaction rate constant can be calculated by the plots of the $\ln(C/C_0)$ *vs.* radiation time (t). The obtained rate law may be $\ln(C/C_0) = -kt$, where C is the concentration of dye, C_0 the initial concentration of dye, k the reaction rate constant, and t the irradiation time. The degradation rate constant k of $ZnGa_2O_4$ nanorods was estimated to be 0.0397 min^{-1}, which was 2.51 times and 4.22 times higher than those of Ga-doped ZnO nanorods (0.0158 min^{-1}) and hexagonal ZnO microdishes (0.0094 min^{-1}), respectively (Fig. 8B). Fig. 8C shows the change of absorption spectra of the RhB solution when exposed to UV light at different times in the presence of the $ZnGa_2O_4$ photocatalyst sample, which clearly shows that the absorption peak of RhB drops gradually with an increase of exposure time to 90 min (confirming the degradation of RhB as shown in Fig. 8A). Furthermore, stability testing on the $ZnGa_2O_4$ sample illustrates that the degradation rate shows slight decrease after four runs of irradiation within 360 min (Fig. 8D). The above mentioned results demonstrate that the obtained $ZnGa_2O_4$ nanorods can be used as a promising photocatalyst with excellent activity and desirable stability for the degradation of RhB in aqueous solution under UV light radiation.

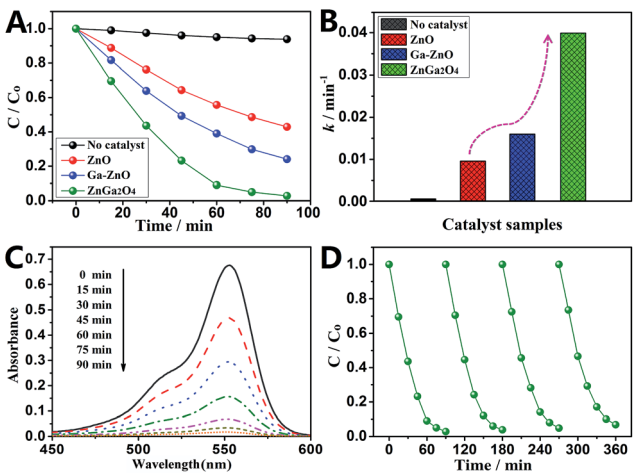

Fig. 8 (A) Photocatalytic activities and (B) rate constant k of RhB degradation for the as-prepared photocatalysts; (C) absorption spectrum of RhB solution and (D) cycling runs for the degradation of RhB in the presence of $ZnGa_2O_4$ photocatalyst under UV light radiation.

The physical dimensions and chemical compositions of semiconductors have significant effects on their physicochemical properties.[1] The smaller dimension of semiconductors often leads to higher photocatalytic activity because of their higher specific surface area along with optimized utilization efficiency.[2] Obviously, the specific surface area of Ga-doped ZnO nanorods (61.2 $m^2\ g^{-1}$) is much higher than that of hexagonal ZnO microdishes (38.4 $m^2\ g^{-1}$). Hence, the improved activity of Ga-doped ZnO nanorods relative to hexagonal ZnO microdishes can be attributed to the high surface area of nanorod structures. However, the specific surface areas of $ZnGa_2O_4$ nanorods (65.7 $m^2\ g^{-1}$) and Ga-doped ZnO nanorods (61.2 $m^2\ g^{-1}$) are more approximate, so the high activity of the $ZnGa_2O_4$ nanorods sample is largely due to its favorable material structures.

It is generally accepted that the superior photocatalytic activity of $ZnGa_2O_4$ originates from its unique electronic and band structures. For one thing, the bottom of the conduction band (LUMO) is formed by Ga4s4p–Zn4s4p hybridized atomic orbits, which promote the mobility of photogenerated electrons and are beneficial for charge separation.[20] For another, the wider band gap (4.4 eV) endows the photogenerated charge with stronger reductive capability, which results in stronger redox ability of the photogenerated electron–hole pairs, thus facilitating the photocatalytic activity.[21] In addition, the possible existence of trace heterojunctions of ZnO–$ZnGa_2O_4$ may contribute to photocatalytic activity by the improved charge transfer. Accurate results are expected by further advanced characterization techniques.

To analyze the catalytic mechanism, the band structures of ZnO and $ZnGa_2O_4$ and possible pathway of RhB photocatalytic degradation are schematically illustrated in Fig. 9. In the case of $ZnGa_2O_4$, the E_{VB} is 3.15 V, which is much higher than the 2.38 V of $E(HO^{\bullet}/OH^{-})$; the E_{CB} is −1.25 V, which is much lower than the −0.33 V of $E(O_2/O_2^{-\bullet})$.[11] In the case of ZnO, only the E_{CB} is lower than that of $E(O_2/O_2^{-\bullet})$. As a result, $HO^{\bullet}$ can be more readily generated for $ZnGa_2O_4$ under UV light in RhB aqueous solution, leading to the $ZnGa_2O_4$ photocatalysts' much higher photocatalytic properties than that of ZnO. The possible reaction process is as follows: once the $ZnGa_2O_4$ catalyst generates

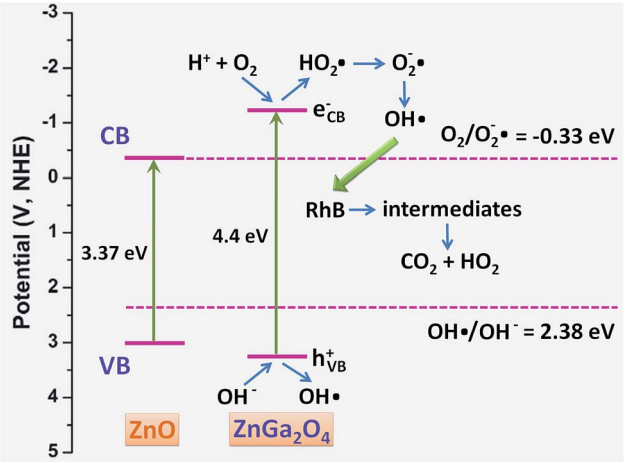

Fig. 9 Schematic illustration for the band structures of ZnO and $ZnGa_2O_4$ and the proposed pathway of RhB photocatalytic degradation.

the electron–hole pairs by UV light radiation, the photogenerated electrons (e^-) on the conduction band (CB) bond with adsorbed oxygen and water to form strong oxidizing species of $O_2^{-\bullet}$ and $HO^\bullet$, while the holes (h^+) on the valence band (VB) also bond with adsorbed oxygen and water to form $HO^\bullet$. Under the action of substantial, strong oxidizing species, the structure of RhB is destroyed and finally decomposed into CO_2 and H_2O. All these processes might be described as follows:[22]

$$e^- + O_2 \rightarrow {}^\bullet O_2^- \quad (1)$$

$${}^\bullet O_2^- + e^- + 2H^+ \rightarrow H_2O_2 \quad (2)$$

$$H_2O_2 + e^- \rightarrow {}^\bullet OH + OH^- \quad (3)$$

$$h^+ + H_2O \rightarrow {}^\bullet OH + H^+ \quad (4)$$

$${}^\bullet OH + RhB \rightarrow CO_2 + H_2O \quad (5)$$

It is well known that plenty of materials have been available for photocatalytic degradation of RhB, including TiO_2,[23] ZnO,[24] AgBr,[25] Ag_3PO_4,[26] BiOBr,[27] $BiPO_4$[28] as well as $ZnGa_2O_4$. TiO_2 is the most extensively studied and stable catalyst for photocatalytic degradation in the scientific perspective. However, it is difficult to determine which of them is the most promising photocatalyst in real-time application, due to their different catalytic mechanisms and the cost of materials. In the present study, we report the controlled synthesis of self-supported $ZnGa_2O_4$ nanorod arrays by using an efficient SLS growth and TMC process associated strategy. Although it is difficult to discuss the superiority of $ZnGa_2O_4$ relative to TiO_2 on the degradation of RhB, the proposed SLS growth and TMC process synthetic strategies may be of general significance in the preparation TiO_2 and other types of photocatalysts.

In conclusion, we demonstrated the controlled synthesis of $ZnGa_2O_4$ nanorod arrays from hexagonal ZnO microdishes for the advanced application of photodegradation in water purification. The as-prepared $ZnGa_2O_4$ sample has highly self-supported, aligned 1-D nanostructures, where $ZnGa_2O_4$ nanorods with 50–80 nm diameter are vertically assembled into microarchitectures without extraneous supporting substrates. The $ZnGa_2O_4$ nanorod arrays showed much higher BET specific surface areas over the hexagonal ZnO microdishes. Due to favorable 1-D nanostructures and unique electronic band structures, the $ZnGa_2O_4$ photocatalyst exhibited a much higher photocatalytic activity relative to the hexagonal ZnO microdishes, in which the degradation rate of RhB can be 4.22 times as high as that of the ZnO photocatalyst. The findings suggest that this newly fashioned architecture of $ZnGa_2O_4$ could be used as a promising photocatalytic material for organic dye degradation.

Acknowledgements

This research was supported by the National Natural Science Foundation of China (21443006, 21173088 and 21105030), Natural Science Foundation of Guangdong Province (S2013040015162), Guangdong Province and Chinese Academy of Sciences Strategic Cooperative Project (2012B090400003), Science and Technology Project of Maoming (2014006) and Doctor Startup Project of School (513086).

Notes and references

1 A. Alivisatos, *J. Phys. Chem.*, 1996, **100**, 13226–13239.
2 Z. Zhuang, Q. Peng and Y. Li, *Chem. Soc. Rev.*, 2011, **40**, 5492–5513.
3 T. Zhai, L. Li, Y. Ma, M. Liao, X. Wang, X. Fang, J. Yao, Y. Bando and D. Golberg, *Chem. Soc. Rev.*, 2011, **40**, 2986–3004.
4 A. Hochbaum and P. Yang, *Chem. Rev.*, 2010, **110**, 527–546.
5 (*a*) T. Wang, Z. Jiao, T. Chen, Y. Li, W. Ren, S. Lin, G. Lu, J. Ye and Y. Bi, *Nanoscale*, 2013, **5**, 7552–7557; (*b*) M. Lv, D. Zheng, M. Ye, J. Xiao, W. Guo, Y. Lai, L. Sun, C. Lin and J. Zuo, *Energy Environ. Sci.*, 2013, **6**, 1615–1622.
6 (*a*) L. Pan, H. Huang, C. Lim, Q. Hong, M. Tse and O. Tan, *RSC Adv.*, 2013, **3**, 3566–3571; (*b*) M. Sun, X. Ma, X. Chen, Y. Sun, X. Cui and Y. Lin, *RSC Adv.*, 2014, **4**, 1120–1127.
7 M. Nischk, P. Mazierski, M. Gazda and A. Zaleska, *Appl. Catal., B*, 2014, **144**, 674–685.
8 C. Zhang, H. Yu, Y. Li, L. Fu, Y. Gao, W. Song, Z. Shao and B. Yi, *Nanoscale*, 2013, **5**, 6834–6841.
9 (*a*) S. Xu and Z. Wang, *Nano Res.*, 2011, **4**, 1013–1098; (*b*) C. Lai, X. Wang, Y. Zhao, H. Fong and Z. Zhu, *RSC Adv.*, 2013, **3**, 6640–6645.
10 (*a*) L. Liu, J. Huang, L. Cao, J. Wu, J. Fei, H. Ouyang, F. Ma and C. Zhou, *Mater. Lett.*, 2013, **95**, 160–163; (*b*) S. Yan, S. Ouyang, J. Gao, M. Yang, J. Feng, X. Fan, L. Wan, Z. Li, J. Ye, Y. Zhou and Z. Zou, *Angew. Chem.*, 2010, **122**, 6544–6548.
11 (*a*) W. Zhang, J. Zhang, Z. Chen and T. Wang, *Catal. Commun.*, 2009, **101**, 781–1785; (*b*) W. Zhang, J. Zhang, X. Lan, Z. Chen and T. Wang, *Catal. Commun.*, 2010, **11**, 1104–1108.

12 M. Zhong, Y. Li, T. Tokizono, M. Zheng, I. Yamada and J. Delaunay, *J. Nanopart. Res.*, 2012, **14**, 804–814.
13 L. Tien, C. Tseng, Y. Chen and C. Ho, *J. Alloys Compd.*, 2013, **555**, 325–329.
14 (*a*) H. Yu and W. Buhro, *Adv. Mater.*, 2003, **15**, 416–419; (*b*) J. Sun, L. Wang and W. Buhro, *J. Am. Chem. Soc.*, 2008, **130**, 7997–8005.
15 Y. Fang, X. Wen and S. Yang, *Angew. Chem.*, 2006, **118**, 4771–4774.
16 A. Qin, X. Zhou, Y. Qiu, Y. Fang, C. Su and S. Yang, *Adv. Mater.*, 2008, **207**, 68–773.
17 S. Yang, C. Ge, Z. Liu, Y. Fang, Z. Li, D. Kuang and C. Su, *RSC Adv.*, 2011, **1**, 1691–1694.
18 (*a*) L. Tian, H. Zou, J. Fu, X. Yang, Y. Wang, H. Guo, X. Fu, C. Liang, M. Wu, P. Shen and Q. Gao, *Adv. Funct. Mater.*, 2010, **20**, 617–623; (*b*) J. Kim, B. Fang, M. Song and J. Yu, *Chem. Mater.*, 2012, **24**, 2256–2264.
19 X. Zhou, Y. Liu, X. Li, Q. Gao, X. Liu and Y. Fang, *Chem. Commun.*, 2014, **50**, 1070–1073.
20 S. Sampath, D. Kanhere and R. Pandey, *J. Phys.: Condens. Matter*, 1999, **11**, 3635.
21 S. Bae, J. Lee, H. Jung, J. Park and J. Ahn, *J. Am. Chem. Soc.*, 2005, **127**, 10802–10803.
22 G. Chen, M. Sun, Q. Wei, Y. Zhang, B. Zhu and B. Dua, *Chem. Soc. Rev.*, 2012, **41**, 782–796.
23 J. Zhang, Z. Zhu, Y. Tang and X. Feng, *J. Mater. Chem. A*, 2013, **1**, 3752–3756.
24 B. Weng, M. Yang, N. Zhang and Y. Xu, *J. Mater. Chem. A*, 2014, **2**, 9380–9389.
25 J. Wang, C. An, J. Liu, G. Xi, W. Jiang, S. Wang and Q. Zhang, *J. Mater. Chem. A*, 2013, **1**, 2827–2832.
26 H. Li, S. Yin, Y. Wang, T. Sekino, S. W. Lee and T. Satoa, *J. Mater. Chem. A*, 2013, **1**, 1123–1126.
27 D. Zhang, J. Li, Q. Wang and Q. Wu, *J. Mater. Chem. A*, 2013, **1**, 8622–8629.
28 C. Pan, J. Xu, Y. Chen and Y. Zhu, *Appl. Catal., B*, 2012, **115–116**, 314–319.